arXiv:0805.3908v2 [cond-mat.mes-hall] 19 Sep 2008

Noname manuscript No.
(will be inserted by the editor)

Models of electron transport in single layer graphene

F. Guinea

Received: date / Accepted: date

Abstract The main features of the conductivity of doped single layer graphene are analyzed, and models for different scattering mechanisms are presented. Many possible dependencies of the cross section on the Fermi wavelength are identified, depending on the type of scattering mechanism. Defects with internal structure, such as ripples, show non monotonous dependencies, with maxima when the Fermi wavelength is comparable to the typical scale of the defect.

1 Introduction.

A great research effort devoted to graphene started after the realization that single layer graphene can be isolated and that the number of carriers can be tuned[1, 2]. The properties of epitaxially grown samples with few graphene layers[3], has also induced a significant activity. Many of the potential applications are related to the design of electronic devices.

We analyze here some topics related to the electronic transport properties of single layer graphene. We do not consider models for the carrier mobility in systems with more than one layer. It is interesting to note in this respect that the mobility of graphite is significantly higher than that of few layer graphene samples[4]. We will also not analyze the interesting topic of the transport properties of undoped graphene.

We restrict ourselves here to doped single layer samples in the diffusive regime, where the mean free path is shorter than the sample size. In this regime, the motion of the carriers can be described semiclassically, and the carrier mobility is determined by the different scattering mechanisms present in the system. If we describe the effects of the scattering events on the carrier distribution function using the Boltzmann equation, which is a reasonable approximation in this limit, the conductivity of graphene is given

---

F. Guinea
Instituto de Ciencia de Materiales de Madrid. Sor Juana Inés de la Cruz 3. E-28049 Madrid. Spain and Donostia International Physics Center (DIPC), Paseo Manuel de Lendizábal 4, San Sebastián, E-20018, Spain
E-mail: paco.guinea@icmm.csic.es

by:

$$\sigma = \frac{e^2}{h} v_{\rm F}^2 N(\epsilon_{\rm F}) \tau(\epsilon_{\rm F}) \tag{1}$$

where $N(\epsilon_{\rm F})$ is the density of states, and $\tau(\epsilon_{\rm F})$ is the scattering time.

We present, in the following section, a brief description of the behavior of the conductivity in single layer graphene, as function of carrier concentration and temperature. Then, we analyze different scattering mechanisms which may limit the mobility at low temperatures.

2 Qualitative behavior of the conductivity in graphene.

2.1 Low temperature limit.

It was realized at an early stage that the conductivity at low temperatures was almost directly proportional to the carrier density[1], and this dependence has been repeatedly confirmed[5]. As, $N(\epsilon_{\rm F}) \propto \sqrt{\rho}$ in graphene, where ρ is the carrier density, this behavior implies that $\tau(\epsilon_{\rm F}) \propto \sqrt{\rho}$. On the other had, for weak local scatterers the Born approximation predicts an inverse scattering time proportional to the density of states, $\tau^{-1} \propto n_{imp} N(\epsilon_{\rm F}) \propto \sqrt{\rho}$, where n_{imp} is the number of scatterers. Inserting this expression in eq.(1), we find that weak scatterers lead to a conductivity which is independent of the carrier density, in contradiction with the observed behavior.

The linear dependence on carrier density of the conductivity implies that the scattering time should increase with density as $\tau(\rho) \propto \sqrt{\rho}$, or, analogously, the cross section of the defects, which in two dimensions is given by a length, should scale as $k_{\rm F}^{-1}$.

The first mechanism proposed compatible with a $\tau \propto \sqrt{\rho}$ dependence was scattering by charged impurities[6, 7]. The Coulomb potential is scale invariant, as it only depends on the product of the charge of the impurity and the electron charge, Ze^2, which can be rendered dimensionless by dividing it by the Fermi velocity. Hence, the cross section should be proportional to the only length scale in the problem, which is the Fermi wavelength, $\lambda_{\rm F} = k_{\rm F}^{-1}$. This dimensional argument[8] remains valid even when screening by the carriers is included, as the Fermi-Thomas screening length is proportional to the Fermi wavelength in graphene. The electronic structure of graphene near a charged impurity has been studied extensively in later times[9, 10, 11], without changing the previous analysis.

A different mechanism which leads to a linear dependence on the Fermi wavelength of the scattering cross section is induced by strong scatterers, such as lattice vacancies[12]. These defects change significantly the local density of states, as they induce partially localized states at the Dirac energy. As reviewed below, the scattering phasehifts cannot be described by the Born approximation[13, 14, 15].

Other mechanisms which lead to deviations from the $\tau^{-1}(\epsilon_{\rm F}) \propto N(\epsilon_{\rm F})$ dependence expected from the Born approximation are scattering by ripples[16] (see also below), and scattering by defects which lead to long range distortions of the lattice, such as dislocations.

2.2 Finite temperature conductivity

The resistivity of single layer graphene rises as function of temperature[17, 18, 19], and deviates significantly from its low temperature value at room temperature.

The coupling to in plane phonons is well understood[20,21]. The phonon band width is ~ 0.2eV. The number of thermally excited phonons at room temperature is too small to explain the observed rise in the resistivity. Single layer graphene can also support out of plane flexural modes, which show a high density of states at low energies. The coupling to the electrons is quadratic on the phonon coordinates, and the resulting scattering rate is also too low to explain the observed temperature dependence of the resistivity[22]. Note that these modes can be pinned by the substrate[23], reducing their density of states at low energies.

The most likely explanation for the temperature dependence of the resistivity is scattering by substrate modes[24]. The most common substrate used in experiments on graphene samples obtained by mechanical cleavage is SiO_2, which is a polar insulator. The electrons in graphene couple to the electric fields induced by the surface polar modes. These modes can be thermally excited at room temperature. A fit using the observed frequencies and dielectric function of SiO_2 gives a good agreement with experimental data[19].

2.3 Effects of the substrate

Localized charges in the substrate lead to Coulomb scattering and modify the low temperature mobility. At finite temperatures, the conductivity depends on the coupling of the carriers to the substrate modes. Hence, the transport properties of single layer graphene are determined, to a large extent, by the substrate and by the general properties of the surrounding environment. Recent experiments show that the conductivity in graphene is modified in samples suspended above the substrate[25,26]. The presence of water molecules can screen charged impurities[27], as well as change the adhesion between the graphene layer and the substrate[28,23]. A detailed investigation of the effects of different substrates will be very helpful for the understanding of the carrier transport in graphene.

3 Scattering processes in graphene

3.1 General framework

In the following, we analyze different scattering mechanisms which may be present in graphene. We first discuss the generalization of the standard partial wave analysis of scattering off local potentials in quantum mechanics to Dirac quasiparticles[29]. The formalism is rather general, and has already been formulated, using different notation, in[30]. Related results can be found in[13,14]. We then apply it to different scattering processes. The continuum model used neglects scattering between the two inequivalent valleys in graphene. We finally give a scheme which takes into account explicitly the lattice structure, and which can be used to study scattering processes where intervalley scattering is significant.

We analyze the phaseshifts induced by a circular potential well in graphene. Using cylindrical coordinates, the Hamiltonian in the clean system can be written as:

$$\mathcal{H} \equiv v_{\mathrm{F}} \begin{pmatrix} 0 & ie^{-i\phi}\partial_r + \frac{e^{-i\phi}}{r}\partial_\phi & 0 & 0 \\ ie^{i\phi}\partial_r - \frac{e^{-i\phi}}{r}\partial_\phi & 0 & 0 & 0 \\ 0 & 0 & 0 & -ie^{i\phi}\partial_r + \frac{e^{i\phi}}{r}\partial_\phi \\ 0 & 0 & -ie^{-i\phi}\partial_r - \frac{e^{-i\phi}}{r}\partial_\phi & 0 \end{pmatrix} \tag{2}$$

where the two first entries correspond to the K point, and the two last ones to the K' point, and we are setting the Fermi velocity $v_{\mathrm{F}} = 1$.

In the following, we study scattering processes which do not induce intervalley transitions. Hence, we need only consider one valley. We write the incoming wave as:

$$\Psi_{in}(\mathbf{r}) \equiv \begin{pmatrix} 1 \\ e^{i\theta_k} \end{pmatrix} e^{i\mathbf{kr}} \equiv \begin{pmatrix} \sum_n i^n J_n(kr) e^{in\theta} e^{-in\theta_k} \\ \sum_n i^{n+1} J_{n+1}(kr) e^{i(n+1)\theta} e^{-in\theta_k} \end{pmatrix} \tag{3}$$

where the angle θ_k defines the direction of the vector $\mathbf{k}$. In the following, we will set $\theta_k = 0$. The incoming current is $j_x^{in} = k, j_y^{in} = 0$.

The outgoing wave is:

$$\begin{aligned} \lim_{|\mathbf{r}| \to \infty} \Psi_{out}(\mathbf{r}) &= \begin{pmatrix} f(\theta) \\ f(\theta) e^{i\theta} \end{pmatrix} \sqrt{\frac{2}{\pi k r}} e^{ikr} \approx \\ &\approx e^{i\pi/4} \begin{pmatrix} \sum_n i^n f_n \left[J_n(kr) + iY_n(kr) \right] e^{in\theta} \\ \sum_n i^{n+1} \left[f_n [J_{n+1}(kr) + iY_{n+1}(kr) \right] e^{i(n+1)\theta} \end{pmatrix} \end{aligned} \tag{4}$$

The outgoing current is $j_x^{out} = \langle \Psi_{out} | \sigma_x | \Psi_{out} \rangle = 2|f(\theta)|^2 \cos(\theta), j_y^{out} = \langle \Psi_{out} | \sigma_y | \Psi_{out} \rangle = 2|f(\theta)|^2 \sin(\theta)$. The differential cross section is $d\sigma(\theta) = (4|f(\theta)|^2)/(\pi k) d\theta$.

In order to obtain eq.(4), we have made the ansatz:

$$f(\theta) = \sum_n f_n e^{in\theta} \tag{5}$$

and we have used the expansion:

$$\begin{aligned} \lim_{kr \to \infty} J_n(kr) &\approx \sqrt{\frac{2}{\pi k r}} \cos\left(kr - \frac{n\pi}{2} - \frac{\pi}{4} \right) \\ \lim_{kr \to \infty} Y_n(kr) &\approx \sqrt{\frac{2}{\pi k r}} \sin\left(kr - \frac{n\pi}{2} - \frac{\pi}{4} \right) \end{aligned} \tag{6}$$

We assume that the scattering defect has a finite radius, r_0. We can write the wavefunctions of an electron with energy $v_{\mathrm{F}} k$ outside this radius as a superposition of terms:

$$\Psi_n(\mathbf{r}) \equiv \begin{pmatrix} \left[J_n(kr) + R_n Y_n(kr) \right] e^{in\theta} \\ i \left[J_{n+1} + R_n Y_{n+1}(kr) \right] e^{i(n+1)\theta} \end{pmatrix} \tag{7}$$

We now write:

$$\Psi_{in}(\mathbf{r}) + \Psi_{out}(\mathbf{r}) = \sum_n \alpha_n \Psi_n(\mathbf{r}) \tag{8}$$

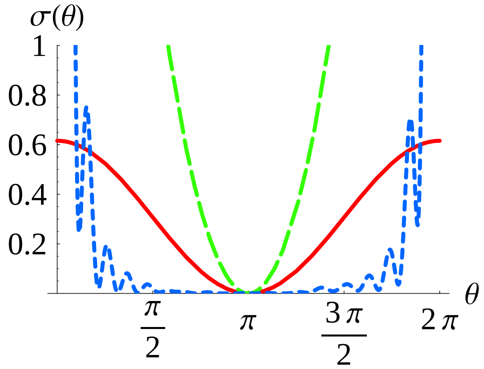

Fig. 1 (Color online). Dependence of the cross section on scattering angle for a circular potential well such that $k'r_0 = 1$. Red: $kr_0 = 0.1 + k'r_0$. Long dashed (green): $kr_0 = 1 + k'r_0$. Short dashed (blue): $kr_0 = 10 + k'r_0$.

And, using eq.(3), eq.(4) and eq.(7), we obtain:

$$\begin{aligned} f_n &= \frac{R_n e^{-i\pi/4}}{i - R_n} \\ f(\theta) &= e^{-i\pi/4} \sum \frac{R_n e^{in\theta}}{i - R_n} \end{aligned} \tag{9}$$

Weak scalar potentials satisfy $R_n = R_{1-n}$. Then, for $\theta = \pi$, we have $f(\theta) = 0$.

3.2 Examples

3.2.1 Potential well

We assume that the potential for $r < r_0$ is V_0. The wavevector of a state with energy $E = v_{\rm F} k$ is $k' = (E + V_0)/v_{\rm F}$. The matching conditions at $r = r_0$ are:

$$\begin{aligned} J_n(kr_0) + R_n Y_n(kr_0) &= T_n J_n(k'r_0) \\ J_{n+1}(kr_0) + R_n Y_{n+1}(kr_0) &= T_n J_{n+1}(k'r_0) \end{aligned} \tag{10}$$

and:

$$R_n = -\frac{J_n(kr_0)J_{n+1}(k'r_0) - J_{n+1}(kr_0)J_n(k'r_0)}{Y_n(kr_0)J_{n+1}(k'r_0) - Y_{n+1}(kr_0)J_n(k'r_0)} \tag{11}$$

The largest values of R_n when $r_0 \rightarrow 0$ are when $n = -1$ and $n = 0$. We expand the Bessel functions, and obtain:

$$\sigma(\theta) \approx \frac{2(k'r_0)^2}{\pi k \log^2(kr_0)} \left[1 - \cos(\theta)\right] \tag{12}$$

The cross section is zero for $\theta = \pi$, in agreement with the suppression of backscattering in the absence of intervalley transitions. Examples of the cross section due to a circular potential are shown in Fig.[1].

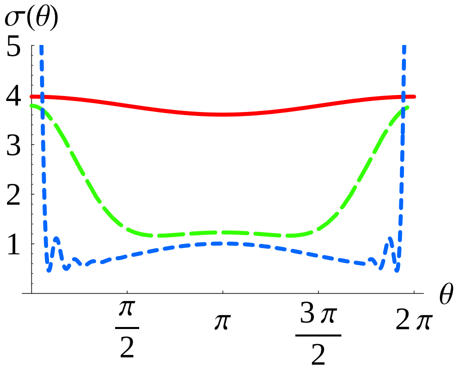

Fig. 2 (Color online). Dependence of the cross section on scattering angle for crack with zigzag edges. Red: $kr_0 = 0.1$. Long dashed (green): $kr_0 = 1$. Short dashed (blue): $kr_0 = 10$.

3.2.2 Circular crack

The boundary conditions for the wavefunction $\Psi(\mathbf{r}) \equiv [\Psi_1(\mathbf{r}), \Psi_2(\mathbf{r})]$ at void with zigzag edges, satisfies $\Psi_1(\mathbf{r}) = 0$. Hence:

$$\begin{aligned} J_n(kr_0) + R_n Y_n(kr_0) &= 0 \\ R_n &= -\frac{J_n(kr_0)}{Y_n(kr_0)} \end{aligned} \tag{13}$$

The largest value of R_n is for $n = 0$. Unlike the previous case, R_0 and R_{-1} are not equal. To lowest order in r_0, the cross section is:

$$\sigma(\theta) \approx \frac{\pi}{8k\left[\log(kr_0/2) + \gamma\right]^2} \tag{14}$$

where γ is the Euler-Mascheroni constant. The scattering probability is isotropic. Examples of the angular dependence of the cross section for a circular crack are shown in Fig.[2]. The behavior of the cross section in this case is the same as that found for a strong scatterer in[31]

3.2.3 Pentagonal cone.

When inserted into a graphene sheet, a pentagon induces a disclination, and a point with finite curvature. The sheet around a pentagon forms a cone. The cone can be attached to a flat sheet with the inclusion of heptagons. We assume that the boundary is sufficiently smooth, so that there is not intervalley scattering. The flat surface is defined for $r \geq r_0$, and the conical region for $r < r_0$. Inside the conical region, the wedge induced by the dislocation is equivalent to a vortex at the apex with flux $\Phi = \pi/3$. The matching conditions are:

$$\begin{aligned} J_n(kr_0) + R_n Y_n(kr_0) &= T_n J_{n+\alpha}(kr_0). \\ J_{n+1}(kr_0) + R_n Y_{n+1}(kr_0) &= T_n J_{n+1+\alpha}(kr_0) \end{aligned} \tag{15}$$

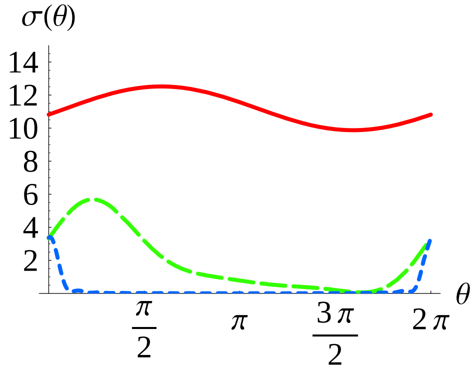

Fig. 3 (Color online). Dependence of the cross section on scattering angle for conical inclusion. Red: $kr_0 = 0.1$. Long dashed (green): $kr_0 = 1$. Short dashed (blue): $kr_0 = 10$.

where $\alpha = -\Phi/(2\pi) = -1/6$. Then:

$$R_n = -\frac{J_n(kr_0)J_{n+1+\alpha}(kr_0) - J_{n+\alpha}(kr_0)J_{n+1}(kr_0)}{Y_n(kr_0)J_{n+1+\alpha}(kr_0) - Y_{n+1}(kr_0)J_{n+\alpha}(kr_0)} \tag{16}$$

The cases n and $1-n$ are not equivalent, and the scattering cross sections at angles θ and $2\pi - \theta$ are not equal. Examples are shown in Fig.[3].

3.3 Weak scatterers. The Born approximation

3.3.1 General framework

We expand the outgoing wave as:

$$\Psi_{out}(\mathbf{r}) \approx \Psi_{in}(\mathbf{r}) + \int d^2\mathbf{r} G_0(\mathbf{r}-\mathbf{r}', \omega)\mathcal{V}(\mathbf{r}')\Psi_{in}(\mathbf{r}') \tag{17}$$

where both $G_0(\mathbf{r}, \omega)$ and $\mathcal{V}(\mathbf{r})$ are 2×2 matrices, and ω is the energy of the particle.

We also have:

$$lim_{r\to\infty} G_0(\mathbf{r}, \omega) = \frac{1}{4\pi^2}\int d^2\mathbf{k}\frac{e^{i\mathbf{kr}}\left(\omega\mathcal{I} + v_{\mathrm{F}}\mathbf{k}\boldsymbol{\sigma}\right)}{\omega^2 - v_{\mathrm{F}}^2\left|\mathbf{k}\right|^2} \sim \frac{\omega e^{i\omega r/v_{\mathrm{F}}}}{v_{\mathrm{F}}^2\sqrt{2\pi\omega r/v_{\mathrm{F}}}}\begin{pmatrix} 1 & e^{i\theta} \\ e^{-i\theta} & 1 \end{pmatrix} \tag{18}$$

where $r = |\mathbf{r}|$. We analyze the scattering from an angle defined by the unit vector $\mathbf{n}'$ into an angle defined by $\mathbf{n}$. Hence, the vector $\mathbf{r}$ is parallel to $\mathbf{n}$. The labels defining the coordinates used for the calculation of the Green's function are sketched in Fig.[4]. The incoming wavefunction is defined in eq.(3). At long distances, $|\mathbf{r}| = r \to \infty$, we can expand:

$$\left|\mathbf{r}-\mathbf{r}'\right| \to r - \mathbf{r}' \bullet \mathbf{n} \tag{19}$$

where $\mathbf{n} = \mathbf{r}/r$. Defining $k_\omega = \omega/v_{\mathrm{F}}$, the Green's function becomes:

$$G(\mathbf{r}-\mathbf{r}', \omega) \approx \frac{k_\omega e^{ik_\omega(r-\mathbf{nr}')}}{v_{\mathrm{F}}\sqrt{2\pi k_\omega r}}\begin{pmatrix} 1 & e^{i\theta} \\ e^{-i\theta} & 1 \end{pmatrix} \tag{20}$$

where θ is the angle approximately given by the direction of $\mathbf{n}$

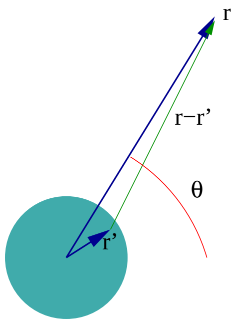

Fig. 4 (Color online). Notation used for the calculation of the Green’s function (see text for details).

3.3.2 Scalar potential

We consider first a potential which does not distinguish the two sublattices:

$$\mathcal{V}(\mathbf{r}) \equiv \begin{pmatrix} V(\mathbf{r}) & 0 \\ 0 & V(\mathbf{r}) \end{pmatrix} \tag{21}$$

The outgoing wave is given by:

$$\begin{aligned} \Psi_{out}(r,\theta) &\equiv \int d^2\mathbf{r}' \frac{k_\omega e^{ik_\omega(r-\mathbf{n}\mathbf{r}')}}{v_{\rm F}\sqrt{2\pi k_\omega r}} \begin{pmatrix} V(\mathbf{r}') & V(\mathbf{r}')e^{i\theta} \\ V(\mathbf{r}')e^{-i\theta} & V(\mathbf{r}') \end{pmatrix} \times e^{ik_\omega \mathbf{n}_{in}\mathbf{r}'} \begin{pmatrix} 1 \\ e^{-i\theta_{in}} \end{pmatrix} \\ &= \frac{k_\omega e^{ik_\omega r}}{v_{\rm F}\sqrt{2\pi k_\omega r}} \int d^2\mathbf{r}' e^{-ik_\omega(\mathbf{n}-\mathbf{n}_{in})\mathbf{r}'} V(\mathbf{r}') \times \begin{pmatrix} 1+e^{i(\theta-\theta_{in})} \\ e^{-i\theta}\left(1+e^{i(\theta-\theta_{in})}\right) \end{pmatrix} \end{aligned} \tag{22}$$

Finally, the amplitude which defines the scattering by an angle $\theta-\theta_{in}$ is:

$$f(\theta-\theta_{in}) \propto \frac{\sqrt{k_\omega}}{v_{\rm F}} \int d^2\mathbf{r}' e^{-ik_\omega(\mathbf{n}-\mathbf{n}_{in})\mathbf{r}'} V(\mathbf{r}') \left[1+e^{i(\theta-\theta_{in})}\right] \tag{23}$$

and the cross section

$$\sigma(\theta-\theta_{in}) \propto \frac{k_\omega}{v_{\rm F}^2} \left| \int d^2\mathbf{r}' e^{-ik_\omega(\mathbf{n}-\mathbf{n}_{in})\mathbf{r}'} V(\mathbf{r}') \right|^2 \left[1+\cos(\theta-\theta_{in})\right] \tag{24}$$

and scattering in the backward direction, $\theta-\theta_{in}=\pi$, is suppressed.

The previous calculation can be easily generalized to a potential:

$$\mathcal{V}(\mathbf{r}) \equiv \begin{pmatrix} \bar{V}(\mathbf{r})+\Delta V(\mathbf{r}) & 0 \\ 0 & \bar{V}(\mathbf{r})-\Delta V(\mathbf{r}) \end{pmatrix} \tag{25}$$

We find:

$$\begin{aligned} f(\theta-\theta_{in}) \propto \frac{\sqrt{k_\omega}}{v_{\rm F}} &\left\{ \int d^2\mathbf{r}' e^{-ik_\omega(\mathbf{n}-\mathbf{n}_{in})\mathbf{r}'} \bar{V}(\mathbf{r}') \left[1+e^{i(\theta-\theta_{in})}\right] \right. \\ &\left. + \int d^2\mathbf{r}' e^{ik_\omega(\mathbf{n}-\mathbf{n}_{in})\mathbf{r}'} \Delta V(\mathbf{r}') \left[1-e^{i(\theta-\theta_{in})}\right] \right\} \end{aligned} \tag{26}$$

The scattering is isotropic, independent of $\theta-\theta_{in}$, when the potential modifies only one sublattice, $\bar{V}(\mathbf{r}) = \pm\Delta V(\mathbf{r})$. Scattering in the forward direction is suppressed when the potential is antisymmetric in the two sublattices, $\bar{V}(\mathbf{r}) = 0$.

3.3.3 Isotropic elastic strains.

An elastic distortion induces a gauge potential[32]:

$$\mathcal{V}(\mathbf{r}) \equiv \begin{pmatrix} 0 & \beta t \left(u_{xx} - u_{yy} + 2iu_{xy} \right) \\ \beta t \left(u_{xx} - u_{yy} - 2iu_{xy} \right) & 0 \end{pmatrix} \tag{27}$$

where u_{ij} are the components of the strain tensor, t is the nearest neighbor hopping term in the tight binding hamiltonian, and $\beta = \partial t / \partial d$, where d is the bond length.

An isotropic ripple with a height profile $h(r)$ leads to (in radial coordinales):

$$\mathcal{V}(r, \phi) \equiv \begin{pmatrix} 0 & \beta t \left(\frac{\partial h}{\partial r} \right)^2 e^{-2i\phi} \\ \beta t \left(\frac{\partial h}{\partial r} \right)^2 e^{2i\phi} & 0 \end{pmatrix} \tag{28}$$

This potential is not isotropic, and the scattering does not depend only on the angle between the incoming and outgoing directions. We define

$$g(r) = \beta t \left(\frac{\partial h}{\partial r} \right)^2 \tag{29}$$

The outgoing wave can be written as:

$$\begin{aligned} \Psi_{out}(r, \theta) \equiv & \int d^2\mathbf{r}' \frac{k_\omega e^{ik_\omega (r + \mathbf{n}\mathbf{r}')}}{v_{\mathrm{F}} \sqrt{2\pi k_\omega r}} \begin{pmatrix} g(r) e^{i(\theta + 2\phi)} & g(r) e^{-2i\phi} \\ g(r) e^{2i\phi} & g(r) e^{i(-\theta - 2\phi)} \end{pmatrix} \times \\ & \times e^{ik_\omega \mathbf{n}_{in} \mathbf{r}'} \begin{pmatrix} 1 \\ e^{-i\theta_{in}} \end{pmatrix} \end{aligned} \tag{30}$$

we can write:

$$(\mathbf{n} - \mathbf{n}_{in}) \mathbf{r}' = |\mathbf{n} - \mathbf{n}_{in}| \, r' \cos(\theta_{n - n_{in}} - \phi) \tag{31}$$

where:

$$\tan(\theta_{n - n_{in}}) = \frac{\sin(\theta) - \sin(\theta_{in})}{\cos(\theta) - \cos(\theta_{in})} = - \cot \left(\frac{\theta + \theta_{in}}{2} \right) \tag{32}$$

so that:

$$\theta_{n - n_{in}} = \frac{\theta + \theta_{in}}{2} - \frac{\pi}{2} \tag{33}$$

we can make the change of variables $\phi = \phi' + (\theta + \theta_{in})/2 - \pi/2$ in the integral over ϕ in eq.(30), and obtain:

$$\begin{aligned} \Psi_{out}(r, \theta) \equiv & \int r' dr' d\phi' \frac{k_\omega e^{ik_\omega (r)}}{v_{\mathrm{F}} \sqrt{2\pi k_\omega r}} e^{ik_\omega |\mathbf{n} - \mathbf{n}'| r' \cos \phi'} g(r') \times \\ & \times \begin{pmatrix} e^{i(2\phi' + 2\theta + \theta_{in} + \pi)} + e^{i(-2\phi' - \theta - 2\theta_{in} - \pi)} \\ e^{i(2\phi' + \theta + \theta_{in} + \pi)} + e^{i(-2\phi' - 2\theta - 2\theta_{in} - \pi)} \end{pmatrix} \\ = & \int dr' \frac{k_\omega e^{ik_\omega (r)}}{v_{\mathrm{F}} \sqrt{2\pi k_\omega r}} J_2(k_\omega |\mathbf{n} - \mathbf{n}'| r') g(r') \times \\ & \times \begin{pmatrix} e^{-i\theta_{in}} \left(e^{2i(\theta + \theta_{in})} + e^{-i(\theta + \theta_{in})} \right) \\ e^{-i\theta} e^{-i\theta_{in}} \left(e^{2i(\theta + \theta_{in})} + e^{-i(\theta + \theta_{in})} \right) \end{pmatrix} \end{aligned} \tag{34}$$

where $J_2(x)$ is a Bessel function. The scattering amplitude can be written as:

$$f(\theta,\theta_{in}) \propto -\frac{\sqrt{k_\omega}}{v_{\rm F}} e^{-i\theta_{in}} \left(e^{2i(\theta+\theta_{in})} + e^{-i(\theta+\theta_{in})} \right) \int dr' J_2(k_\omega |\mathbf{n}-\mathbf{n}'| r') g(r') \tag{35}$$

and the cross section is:

$$\sigma(\theta,\theta_{in}) \propto \frac{k_\omega}{v_{\rm F}^2} \left| \int dr' J_2(k_\omega |\mathbf{n}-\mathbf{n}'| r') g(r') \right|^2 \{1+\cos[3(\theta+\theta_{in})]\} \tag{36}$$

This function reflects the threefold symmetry of the honeycomb lattice.

Near the Dirac point, $|k_\omega| \to 0$, the cross section in eq.(36) grows as $|k_\omega|^3$. For a ripple of height h and size l, we have:

$$g(r) \approx \beta t \times \begin{cases} \left(\frac{h}{l}\right)^2 & r \ll l \\ 0 & r \gg l \end{cases} \tag{37}$$

The hopping t is given approximately, by $t \approx v_{\rm F}/a$, where a is the interatomic distance. The total cross section, obtained by integrating eq.(36) over angles is given by:

$$\sigma \sim \begin{cases} \frac{\beta^2 h^4 k_\omega (k_\omega l)^4}{a^2} & k_\omega l \ll 1 \\ \frac{\beta^2 h^4 k_\omega}{a^2} & k_\omega l \sim 1 \\ \frac{\beta^2 h^4 k_\omega}{a^2 (k_\omega l)^4} & k_\omega l \gg 1 \end{cases} \tag{38}$$

The total cross section has a maximum for $k_\omega \sim l^{-1}$, $\sigma_{max} \sim (\beta t/v_{\rm F})^2 h^4/l$. For $h \sim 1$nm and $l \sim 10$nm, we obtain $\sigma_{max} \sim 10h \sim 10$nm.

3.3.4 Effective magnetic vortex

Topological lattice defects, such as disclinations and dislocations induce, in addition to long range strains, an effective vortex at their core[33,34,35], which mixes the two valleys in the case of a disclination. We consider now the scattering by such a vortex alone, neglecting the effect of the elastic strains. An isotropic distribution of a (fictitious) magnetic field induces a potential:

$$\mathcal{V}(r,\phi) \equiv \begin{pmatrix} 0 & g(r)e^{i\phi} \\ g(r)e^{-i\phi} & 0 \end{pmatrix} \tag{39}$$

where $g(r) \propto (e/c) v_{\rm F} r B(r)$. Using the same scheme as in the previous case, we find:

$$\begin{aligned} \Psi_{out}(r,\theta) \equiv & \int d^2\mathbf{r}' \frac{k_\omega e^{ik_\omega (r+\mathbf{n}\mathbf{r}')}}{v_{\rm F}\sqrt{2\pi k_\omega r}} \begin{pmatrix} g(r)e^{i(\theta-\phi)} & g(r)e^{i\phi} \\ g(r)e^{-i\phi} & g(r)e^{i(-\theta+\phi)} \end{pmatrix} \times \\ & \times e^{ik_\omega \mathbf{n}_{in}\mathbf{r}'} \begin{pmatrix} 1 \\ e^{-i\theta_{in}} \end{pmatrix} = \\ & = i \int dr' \frac{k_\omega e^{ik_\omega (r)}}{v_{\rm F}\sqrt{2\pi k_\omega r}} J_1(k_\omega |\mathbf{n}-\mathbf{n}'| r') f(r') \times \\ & \times \begin{pmatrix} e^{i(\theta-\theta_{in}+\pi)/2} + e^{i(\theta-\theta_{in}+\pi)/2} \\ e^{-i(\theta+\theta_{in}+\pi)/2} + e^{-i(\theta+\theta_{in}-\pi)/2} \end{pmatrix} \end{aligned} \tag{40}$$

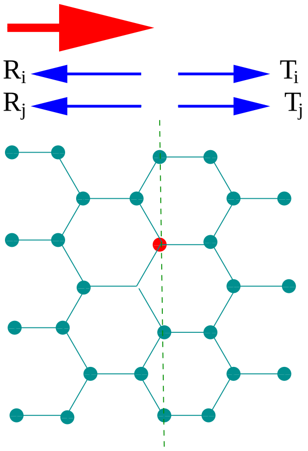

Fig. 5 (Color online). Geometry used to calculate scattering amplitudes in the discrete honeycomb lattice. See text for details.

so that:

$$f(\theta-\theta_{in}) \propto e^{i(\theta-\theta_{in})/2}\frac{\sqrt{k_\omega}}{v_{\rm F}}\int dr' J_1(k_\omega|\mathbf{n}-\mathbf{n}'|r')g(r') \tag{41}$$

We assume that:

$$g(r) \approx \begin{cases} f\times\frac{v_{\rm F}\Phi_0}{l} & r \ll l \\ 0 & r \gg l \end{cases} \tag{42}$$

where f is a dimensionless number of order unity, Φ_0 is the flux quantum, and l is the redius of the distorted region, we find that the total cross section behaves as:

$$\sigma(k_\omega) \sim \begin{cases} k_\omega f^2 l^2 (k_\omega l)^3 & k_\omega l \ll 1 \\ k_\omega f^2 l^2 & k_\omega l \sim 1 \\ \frac{k_\omega f^2 l^2}{(k_\omega l)^3} & k_\omega l \gg 1 \end{cases} \tag{43}$$

3.4 Lattice effects.

3.4.1 Green's function formulation

We can generalize the previous analysis to the discrete honeycomb lattice. The scattering is no longer isotropic, and only some incident angles can be studied analytically. We fix the direction of the incident wave, and use periodic boundary conditions in the perpendicular direction. A particular case, where the incident wave is along one of the symmetry axes of the honeycomb lattice is sketched in Fig.[5]. The analysis requires the calculation of the transmission and reflection coefficients for the different channels in the problem. The scheme can easily be generalized to any local lattice defect, as sketched in Fig.[6]. This scheme, using the continuum approximation for the local Green's function, has been discussed in[31]. The scattering process can be solved if the amplitudes of the reflected and transmitted waves along each of the transverse channels of the lattice can be determined. We label the transverse channels by the angular momentum $k_\perp$. Using periodic boundary conditions with N unit cells in the transverse direction, the allowed values of $k_\perp$ are $k_\perp = 2\pi n/(Na), n = 0, \cdots, N-1$; a is the lattice constant.

We analyze next the scattering by a local impurity, and then extend the calculation to more complex lattice defects.

3.4.2 Scattering by an impurity.

A local impurity perturbs only one site of the lattice. The matching of the incoming and the reflected and transverse waves needs only be defined along a line of sites which includes the vacancy. We assume that the incoming wave has $k_\perp^0 = 0$. There are N reflection and transmission amplitudes, $R_{k_\perp}, T_{k_\perp}$. The continuity of the wavefunctions allows us to define N equations:

$$\begin{aligned} 1 + R_0 &= T_0 \\ R_{k_\perp} &= T_{k_\perp} \qquad k_\perp \neq 0 \end{aligned} \tag{44}$$

The other N equations needed to determine uniquely the values of $R_{k_\perp}, T_{k_\perp}$ are given by the condition that the full wavefunction must be an eigenvector with energy ϵ: We use eq.(44) in order to eliminate the $R_{k_\perp}$, and obtain:

$$\begin{aligned} G_0^{-1}(k_\perp, 0, \epsilon) \times T_{k_\perp} &= G_0^{-1}(k_\perp, 0, \epsilon) + V \sum_{k'_\perp} G_0(k'_\perp, 0, \epsilon) \qquad k_\perp = 0 \\ G_0^{-1}(k_\perp, 0, \epsilon) \times T_{k_\perp} &= V \sum_{k'_\perp} G_0(k'_\perp, 0, \epsilon) \qquad k_\perp \neq 0 \end{aligned} \tag{45}$$

where V is the strength of the impurity potential, and:

$$G_0(k_\perp, 0, \omega) = \sum_{k_\parallel} \frac{1}{\omega - \epsilon(k_\parallel, k_\perp)} \tag{46}$$

is the Green's function of the problem, resolved in transverse momentum, and projected on the row where the impurity is located. The energies $\epsilon(k_\parallel, k_\perp)$ correspond to the unperturbed hamiltonian.

The solution of eq.(45) is:

$$\begin{aligned} T_{k_\perp} &= 1 + \frac{V G_0(k_\perp, 0, \epsilon)}{1 - V \sum_{k'_\perp} G_0(k'_\perp, 0, \epsilon)} \qquad k_\perp = 0 \\ T_{k_\perp} &= \frac{V G_0(k_\perp, 0, \epsilon)}{1 - V \sum_{k'_\perp} G_0(k'_\perp, 0, \epsilon)} \qquad k_\perp \neq 0 \end{aligned} \tag{47}$$

At low energies, we can write:

$$\epsilon(k_\parallel, k_\perp) \approx v_{\mathrm{F}} \sqrt{k_\parallel^2 + k_\perp^2} \tag{48}$$

and:

$$
\begin{aligned}
G_0(k_\perp, 0, \omega) &\approx \frac{k_\parallel}{v_{\mathrm{F}}\sqrt{k_\parallel^2 + k_\perp^2}} \approx \frac{1}{v_{\mathrm{F}}\cos(\theta)} \\
\sum_{k'_\perp} G_0(k'_\perp, 0, \epsilon) &\approx \frac{\sqrt{k_\parallel^2 + k_\perp^2}}{v_{\mathrm{F}}}\left[i + \log\left(\frac{\Lambda}{\sqrt{k_\parallel^2 + k_\perp^2}}\right)\right]
\end{aligned} \tag{49}
$$

where Λ is a high momentum cutoff of the order of the inverse of the lattice constant, $\Lambda \sim a^{-1}$.

In order to obtain the total transmitted current as function of the incoming current one must multiply $|T_{k_\parallel}|^2$ by the outgoing current, $j_{k_\parallel}$ and divide it by the ingoing current, j_0. In the tight binding model which describes each transverse channel, we have that $j_\parallel = G_0^{-1}(k_\perp, 0, \omega)$. Hence, we can write for the cross section:

$$
\sigma(k_\parallel, \epsilon) \propto \frac{G_0(k_0, \epsilon) V^2 G_0(k_\parallel, \epsilon)}{|1 - V \sum_{k'_\perp} G_0(k'_\perp, 0, \epsilon)|^2} \tag{50}
$$

and, in order to obtain the dependence of the cross section on the outgoing angle, θ, we must take into account that:

$$
\sigma(\theta, \epsilon) d\theta = \sigma(k_\parallel) dk_\parallel = \sigma(k_\parallel, \epsilon)\sqrt{k_\parallel^2 + k_\perp^2}\cos(\theta) d\theta \tag{51}
$$

Using these expressions, we find that the scattering by a lattice impurity is isotropic at low energies, and valley independent (note that the calculation does not distinguish the valley index of the transmitted wave) . For $V \ll t$, where t is the nearest neighbor hopping, the total cross section is given, approximately, by:

$$
\sigma \sim \frac{\sqrt{k_\parallel^2 + k_\perp^2} V^2 a^4}{v_{\mathrm{F}}^2} \tag{52}
$$

and, for $V \gg t$, we find, neglecting logarithmic corrections:

$$
\sigma \sim \frac{1}{\sqrt{k_\parallel^2 + k_\perp^2}} \tag{53}
$$

In agreement with the results obtained for a crack in the continuum limit, eq.(14).

4 Conclusions

We have analyzed scattering processes which will affect the mobility of carriers in graphene. We show that localized defects can be classified into at least two types with opposite dependence of the cross section on density: i) weak scatterers, where the cross section grows as the square root of the density, and strong scatterers, where the cross section decreases as the square root of the density. The resulting conductivity can be either density independent, or grow linearly with density.

We have also studied defects with internal structure, such as those induced by elastic strains or ripples, where the perturbation couples to the Dirac quasiparticles as

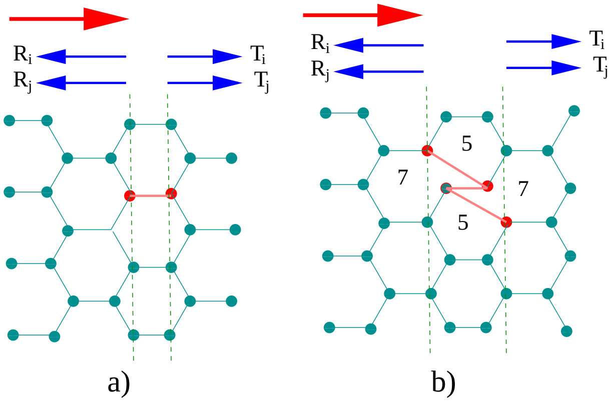

Fig. 6 (Color online). Geometry used to calculate scattering amplitudes in the discrete honeycomb lattice in the presence of bond disorder. Left: perturbation of a single bond. Right: Stone-Wales defect. See text for details.

an effective gauge field. We find that for ripples with a characteristic size l, the cross section is highest for a density such that $k_F^{-1} \sim l$. The scattering at each valley does not show a symmetry between θ and $-\theta$, where θ is the incident angle, as expected from general symmetry considerations.

We have finally shown that the classification of short range potentials into weak and strong scatterers with different dependence on carrier density remains unchanged, even when intervalley scattering is important.

5 Acknowledgements

This work was supported by MEC (Spain) through grant FIS2005-05478-C02-01, the Comunidad de Madrid, through the program CITECNOMIK, CM2006-S-0505-ESP-0337, and the European Union Contract 12881 (NEST).

References

1. K.S. Novoselov, A.K. Geim, S.V. Morozov, D. Jiang, Y. Zhang, S.V. Dubonos, I.V. Grigorieva, , A.A. Firsov, Science **306**, 666 (2004)
2. K.S. Novoselov, D. Jiang, F. Schedin, T.J. Booth, V.V. Khotkevich, S.V. Morozov, A.K. Geim, Proc. Natl. Acad. Sci. U.S.A. **102**, 10451 (2005)
3. C. Berger, Z. Song, T. Li, X. Li, A.Y. Ogbazghi, R. Feng, Z. Dai, A.N. Marchenkov, E.H. Conrad, P.N. First, W.A. de Heer, J. Phys. Chem. Sol. **108**, 19912 (2004)
4. N. García, P. Esquinazi, J. Barzola-Quiquia, B. Ming, D. Spoddig, (2008). ArXiv:0803.2203
5. Y.W. Tan, Y. Zhang, K. Bolotin, Y. Zhao, S. Adam, E. Hwang, S. Das Sarma, H.L. Stormer, P. Kim, Phys. Rev. Lett. **99**, 246803 (2007)
6. K. Nomura, A.H. MacDonald, Phys. Rev. Lett. **98**, 076602 (2007)
7. S. Adam, E.H. Hwang, V. Galitski, S. Das Sarma, Proc. Natl. Acad. Sci. USA **104**, 18392 (2007)
8. I appreciate helpful exchanges with D. S. Novitov on this topic.
9. A.V. Shytov, M.I. Katsnelson, L.S. Levitov, Phys. Rev. Lett. **99**, 236801 (2007)
10. M.M. Fogler, D.S. Novikov, B.I. Shklovskii, Phys. Rev. B **76**, 233402 (2007)
11. V.M. Pereira, J. Nilsson, A.H. Castro Neto, Phys. Rev. Lett. **99**, 166802 (2007)

12. V.M. Pereira, F. Guinea, J.M.L. dos Santos, N.M. Peres, A.H. Castro Neto, Phys. Rev. Lett. **96**, 036801 (2006)
13. M.I. Katsnelson, K.S. Novoselov, Solid State Commun. **143**, 3 (2007)
14. M. Hentschel, F. Guinea, Phys. Rev. B **76**, 115407 (2007)
15. T. Stauber, N.M.R. Peres, F. Guinea, Phys. Rev. B **76**, 205423 (2007)
16. M.I. Katsnelson, A.K. Geim, Phil. Trans. R. Soc. A **366**, 195 (2008)
17. Y.W. Tan, Y. Zhang, H.L. Stormer, P. Kim, Eur. Phys. J.-Special Topics **148**, 19 (2007)
18. S.V. Morozov, K.S. Novoselov, M.I. Katsnelson, F. Schedin, D.C. Elias, J.A. Jaszczak, A.K. Geim, Phys. Rev. Lett. **100**, 016602 (2008)
19. J.H. Chen, C. Jang, S. Xiao, M. Ishigami, M.S. Fuhrer, Nature Nanotechnol. **3**, 2006 (2008)
20. F. Guinea, J. Phys. C **14**, 3345 (1981)
21. E.H. Hwang, S. Das Sarma, (2007). ArXiv:0711.0754
22. E. Mariani, F. von Oppen, Phys. Rev. Lett. **100**, 076801 (2007)
23. J. Sabio, C. Seoánez, S. Fratini, F. Guinea, A.H. Castro Neto, F. Sols, Phys. Rev. B **77**, 195409 (2008)
24. S. Fratini, F. Guinea, Phys. Rev. B **77**, 195415 (2008)
25. K.I. Bolotin, K.J. Sikes, Z. Jiang, G. Fudenberg, J. Hone, P. Kim, H.L. Stormer, (2008). ArXiv:0802.2389
26. X. Du, I. Skachko, A. Barker, E.Y. Andrei, (2008). ArXiv:0802.2933
27. F. Schedin, A.K. Geim, S.V. Morozov, D. Jiang, E.H. Hill, P. Blake, K.S. Novoselov, Nature Mat. **6**, 652 (2007)
28. J. Moser, A. Verdaguer, D. Jiménez, A. Barreiro, A. Bachtold, Appl. Phys. Lett. **92**, 123507 (2008)
29. L.D. Landau, L.M. Lifschitz, *Quantum Mechanics: Non-Relativistic Theory, Volume 3* (Elsevier, 1958)
30. D.S. Novikov, Phys. Rev. B **76**, 245435 (2007)
31. P.M. Ostrovsky, I.V. Gornyi, A.D. Mirlin, Phys. Rev. B **73**, 235443 (2006)
32. J.L. Mañes, Phys. Rev. B **76**, 045430 (2007)
33. J. González, F. Guinea, M.A.H. Vozmediano, Phys. Rev. Lett. **69**, 172 (1992)
34. J. González, F. Guinea, M.A.H. Vozmediano, Nucl. Phys. B **406 [FS]**, 771 (1993)
35. A. Morpurgo, F. Guinea, Phys. Rev. Lett. **97**, 196804 (2006)